

An Instantaneous Center of Rotation-Based Extended Kalman Filter Approach for the On-Line Estimation of Wheelchair Tire Slip

Kelilah L. Wolkowicz¹ Jesse L. Pentzer² Christopher X. Miller¹ Jason Z. Moore¹ Sean N. Brennan^{1*}

¹Mechanical Engineering Department

The Pennsylvania State University
University Park, PA 16802

²Applied Research Lab

The Pennsylvania State University
University Park, PA 16802

ABSTRACT

Wheelchair tire slip is a dangerous scenario that can result from powered wheelchair operation on icy or low-friction surfaces. This research applies instantaneous centers of rotation (ICR) estimation to a wheelchair application where ICR values should rarely change. Changes in these estimates are used to understand the occurrence of slip and to predict motion during that slip. Using inputs of position and orientation obtained through laser odometry, an Extended Kalman Filter (EKF) algorithm is implemented to estimate the changes in wheelchair ICR location estimates that are indicative of slippage. The algorithm is verified via simulation and experimentation using a robotic wheelchair. It is observed that the convergence of the ICR EKF is heavily dependent on the motion history of the wheelchair. Experiments show that ICR locations do not vary significantly under the slip-free conditions of normal operation with 2- σ standard deviations of 0.076 m, but the ICR locations deviate up to 0.84 m during slippage.

1 Introduction

A wheelchair user makes her way down an icy sidewalk in winter in a small town in the northeastern United States. One of her wheels catches an ice patch and, for a terrifying instant, she loses control of her wheelchair. While this scenario may not be able to be completely avoided, the motion of wheelchair tires on slippery surfaces can be predicted, enabling warning systems and safe operational modes that can enhance the safety of wheelchair users. As described by Wang, *et al.*, the loss of control and injury among electric wheelchair users is far too prevalent [1–3]. With over three million wheelchair users in

*Address all correspondence to sbrennan@psu.edu.

the United States, and that number growing, it is increasingly necessary to design and evaluate safety features for electric wheelchair operation [4].

Wheelchair users already face limited mobility. However, wintry and rainy conditions present further mobility constraints [5–7]. Of the 100,000 wheelchair-related accidents reported in 2003, 65 to 80% were attributed to tips and falls, many of which were likely due to slippery or uneven terrain [1, 8]. This increased limitation is particularly worrisome because lack of mobility also contributes to social isolation and psychosocial problems [7]. Unfortunately, little research is devoted to improving the control of wheelchair motion on low-friction surfaces [1, 7, 9].

1.1 Prior Work Detecting Ground Robot Wheel Slip

While encoders can be used to compare the drive wheel speeds to the caster wheel speeds in order to estimate wheel slip for many vehicles, standard electric wheelchairs are limited because they do not typically come equipped with encoders and, therefore, lack the redundant encoder systems required to repeat this estimation [1, 10]. However, most electric wheelchairs being used for research purposes are modified to have encoders and, consequently, are enabled to have odometry measurements and slip detection. For example, Wang, *et al.*, expanded upon the limited control technologies available to electric wheelchairs by installing caster wheel encoders to evaluate the effects of three control algorithms on wheelchair driving speed variation and wheel slip: model-based control, proportional-integral-derivative (PID) control, and open-loop control. Wheel slip was detected by comparing the wheelchair velocity obtained from a caster-wheel encoder with the wheelchair wheel velocities obtained from the drive wheel encoders. Of the three control algorithms tested, experimental results determined that the model-based control platform yielded the best results. With model-based control, the slip coefficient could be made to be similar at different driving speeds because the algorithm decreased the driving wheel speed when slip exceeded a predefined threshold to increase traction. The researchers suggest that a rapid method for detecting changes in terrain may be helpful for setting terrain-specific slip coefficient control thresholds.

A study by Lemaire, *et al.*, evaluated wheelchair navigation strategies for ramp ascent and descent for winter weather conditions [7]. Their experimental conditions included several ramp grades with: (i) packed snow and (ii) packed snow with a freezing rain cover and traction grit. While the study focused on manual wheelchair users, it was confirmed that further research on mobility in winter is necessary. In particular, it was observed that independence cannot be assumed for all conditions using standard propulsion techniques alone.

Mobile robot slip estimation is a well-studied area of research. A standard technique is to compare movement inputs with measured motion. This approach can be accomplished using wheel encoder odometry, visual odometry, inertial measurement units (IMUs), laser rangefinder sensors, and/or high fidelity position systems, including global positioning systems (GPS). Previous research in the field of robotics has addressed slip detection using exteroceptive or absolute sensors either individually or in combination [11–13]. Visual odometry and IMU measurements can be fused through a Kalman Filter pose estimator for slippage detection, and this approach was demonstrated on a Mars rover in the work of Helmick, *et al.* [11]. The merged estimate was compared to full vehicle kinematic algorithm estimates to determine if and how much slippage occurred. Similarly, Olsen, *et al.*, combined visual odometry with absolute heading measurements for long-range robot

navigation [12]. This technique combined feature selection and tracking with orientation sensor measurements to reduce the accumulation of odometry error over long distances.

Longitudinal wheel slip and immobilized conditions can also be estimated from measurements derived from wheel encoders, IMU, and GPS. Ward, *et al.* integrated this approach with an Extended Kalman Filter (EKF) for a tire traction and braking model to calculate vehicle dynamic forces [14, 15]. Their work demonstrated accurate immobilization detection in the absence of GPS and suggested possible applications in both terrestrial and space robotics.

Reina, *et al.*, proposed another approach to detect slippage that relies purely on proprioceptive sensors [13]. Readings from encoders, a gyroscope, and current sensors were compared for wheel slippage identification on sandy nonflat terrain, for which 61 to 94% of vehicle slippage occurrences were detected. This work also incorporated a visual sinkage estimation algorithm that used a camera to view the wheel-terrain interface. Reina, *et al.* determined the contact angle by attaching a pattern of equally spaced concentric black circumferences on a white background to the wheel. This technique resulted in maximum errors below 15%. While the methods employed by Reina, *et al.*, did not require *a priori* information about the environment, they were limited to detecting slippage along the longitudinal direction of motion.

Vision-based algorithms have been used with increasing regularity to detect slip via stereo or monocular vision odometry [16–18]. Milella, *et al.*, implemented two methods for rough terrain mobile robots using visual inputs [16]. The first method employed a stereovision algorithm for real-time six degree-of-freedom ego-motion estimation, while the second method estimated wheel sinkage of a mobile robot on sandy soil based on edge detection. Nister, *et al.*, presented a system that determines the motion of a stereo head for which no prior knowledge of the scene or the motion is necessary [17]. The method was successfully applied to video from aerial, automotive, and handheld platforms. Preliminary work by Song, *et al.*, integrated a Kalman Filter optical flow method to measure the velocity of mobile robots using a downward-looking camera [18]. This technique was used to track salient natural features on terrain surfaces and provide estimates of vehicle pose and velocity. Estimates from the optical flow algorithm and wheel angular velocities obtained from wheel encoders were then implemented with a sliding mode observer and EKF to estimate longitudinal slip values and slip angle [19].

For many applications, including indoor wheelchair applications, GPS measurements, inertial navigational systems (INS), and other absolute positioning is unavailable. To account for the lack of absolute position measurements, Rogers-Marcovitz, *et al.*, combined Integrated Perturbative Dynamics (IPD) and an EKF to identify systematic and stochastic models of wheel slip [20]. The EKF algorithm implemented in the research of Rogers-Marcovitz, *et al.*, was tested on a tracked vehicle, the Foster-Miller TALON, which relies on slippage for turning maneuvers.

1.2 Prior Work Using ICRs for Ground Robotics

The prior work of Pentzer, *et al.*, focused on motion prediction for skid-steer mobile robots using the track instantaneous center of rotation (ICR) locations [21, 22]. The ICR of a rigid body in planar motion is the location at which the relative velocity of the body to the ICR point is zero at a particular instant of time [23]. At that instant, all other points on the rigid body exhibit pure rotation about the ICR. While both differential-drive and skid-steer vehicles produce rotational motion by adjusting right and left tire or track speeds, skid-steer vehicles rely solely on track or wheel slippage for turning maneuvers.

Consequently, it was determined that ICR kinematics can provide accurate open-loop motion estimates for both differential drive and skid-steer vehicles when they are operated at low speeds on flat, hard terrain [21,22,24]. The further implementation of an EKF enabled the ICR locations to be accurately estimated. The EKF also provided a mapping from the vehicle wheel or track speeds to the vehicle's forward and angular velocity. This technique allows odometry accuracy to be improved even in the absence of GPS measurements, which can ultimately enhance model-based motion prediction for skid-steer robots. The algorithm was particularly innovative in that it can take inputs of orientation or angular rate from a variety of sensors, including GPS, IMU, laser rangefinder, or camera-based measurements to predict accurate ICR locations.

Minimal work has been completed that identifies instances when a wheelchair undergoes slip. This research expands upon the implementation of the algorithm used by Pentzer, *et al.*, and Wolkowicz, *et al.*, to better predict the motion of wheelchairs on icy or low-friction surfaces, often representative of dangerous conditions [21, 22, 25]. In addition, this prior work suggests methods to improve the control of wheelchair motion on slippery surfaces, the ultimate goal of which would enable warning systems and safe operation modes to enhance the safety of wheelchair users.

1.3 ICR EKF Approach for Detecting Wheelchair Slip

The key contribution of this paper is the application of ICR estimation to situations where ICR locations should not change, which is not how they have typically been considered in prior work. Additionally, this work uses these estimates to predict wheelchair motion during slippage. In the work of Pentzer, *et al.*, the application is for bomb-disposal robots whose normal driving environments are almost solely slip-inducing (i.e. skid-steer robots operating on hills, sand, etc.). Wheelchair driving conditions are far more constrained to where slip estimation can be a diagnostic tool. This emphasis on ICR measurement for diagnostics, i.e., assuming a wheelchair should never experience slip, has not been presented in the literature. However, in the instances that a wheelchair does experience slip, this paper contributes an implementation of a practical real-time algorithm that detects wheelchair tire slip while it occurs, utilizes changes in these estimates to understand the occurrence of slip, and presents a model-based framework to predict motion during that slip. The method employed detects lateral and longitudinal slippage. An EKF-based approach is incorporated for which position and orientation are obtained through laser odometry via measurements from a LiDAR laser rangefinder. The current work focuses on a two-wheeled robotic wheelchair system and aims to combine odometry, velocity, and heading measurements to estimate when slippage occurs. While the use of these measurements for slip has previously been applied to skid-steer robotics, it is the implementation of the presented method for nominally slip-free wheelchair-based applications that makes this work novel.

A block diagram representing the flow of the system architecture is illustrated in Fig. 1. The user supplies motion commands via a joystick to the wheelchair system to obtain the desired position, orientation, and individual wheel velocities. The wheelchair system's measured states are sensed via odometry. More accurate measurements of the wheelchair's position and yawrate are also obtained via LiDAR laser odometry. The individual wheel velocities and laser odometry position and orientation measurements are then used as inputs into the ICR EKF. The outputs of the EKF are the wheelchair ICR location estimates that are indicative of slippage, as well as updated measurements of wheelchair position and orientation.

The purpose of this work is to detect wheelchair tire slip in real-time using an ICR EKF-based approach in order

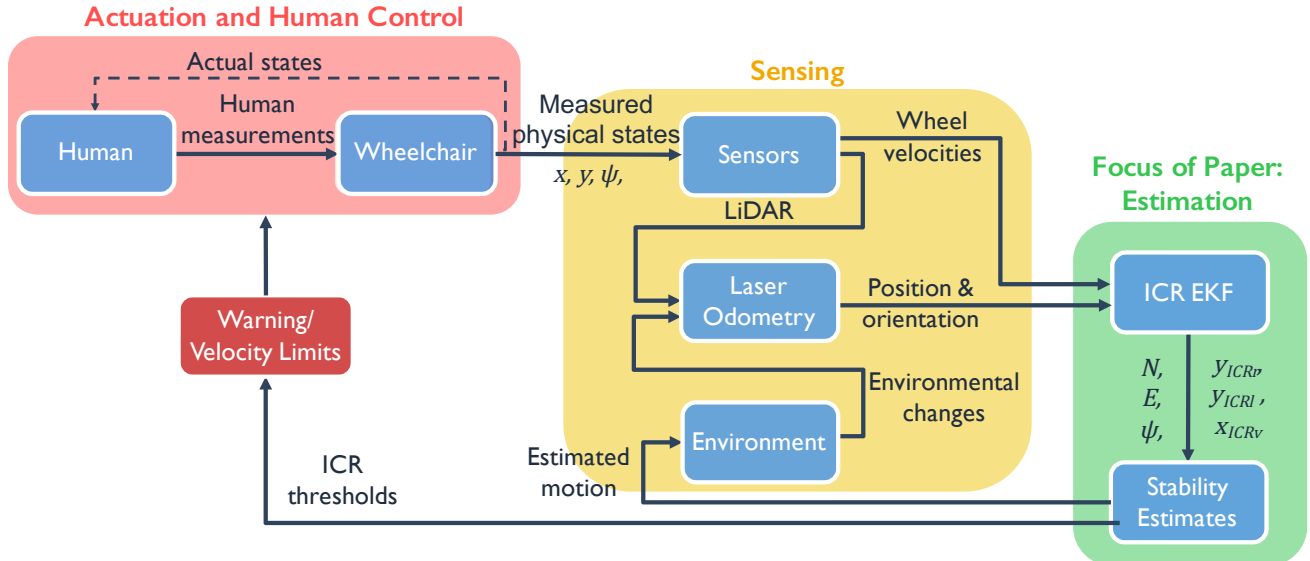


Figure 1: Block diagram representing the signal flow of the system architecture.

to enhance the safety of electric wheelchair operation. The following topics are discussed in subsequent sections: ICR kinematic equations (Section 2); EKF applied to estimate ICR locations (Section 3); verification of algorithm by simulation (Section 4); design of the robotic wheelchair platform used during experimentation (Section 5); results and discussion of experimentation (Section 6 and Section 7); summary of this work and its contributions (Section 8).

2 ICR Kinematics

When applying the kinematic equations to a mobile robot system, several key assumptions are typically made: 1) the robot is traversing flat terrain, 2) there is no tire deformation, and 3) no slipping occurs at the contact point between the drive wheels and the ground surface [26]. While these assumptions may greatly simplify most kinematic analyses, the assumptions also introduce error when applied to scenarios representative of real-world operating conditions, including wintry and rainy weather conditions.

This section introduces the ICR kinematic equations presented in [21, 22, 24, 27]. The kinematic equations are applied to a robotic wheelchair system and used to enhance the wheelchair's predicted motion when the typical kinematic assumptions fail. First, the lateral and longitudinal ICR locations for the wheelchair's right wheel, left wheel, and chassis are presented in terms of the right and left wheel velocities. Subsequently, the calculations for the wheelchair's longitudinal, lateral, and angular velocities are defined. For a two-wheeled robot such as a wheelchair, the true ICR locations should lie directly beneath the drive wheels.

The ICR locations relative to the wheelchair with positive X in the forward direction, positive Y to the right, and positive Z down, are illustrated in Fig. 2 (a). The lateral ICR location between wheelchair body and the ground, y_{ICRv} , is given by:

$$y_{ICRv} = \frac{v_x}{\omega_z}, \quad (1)$$

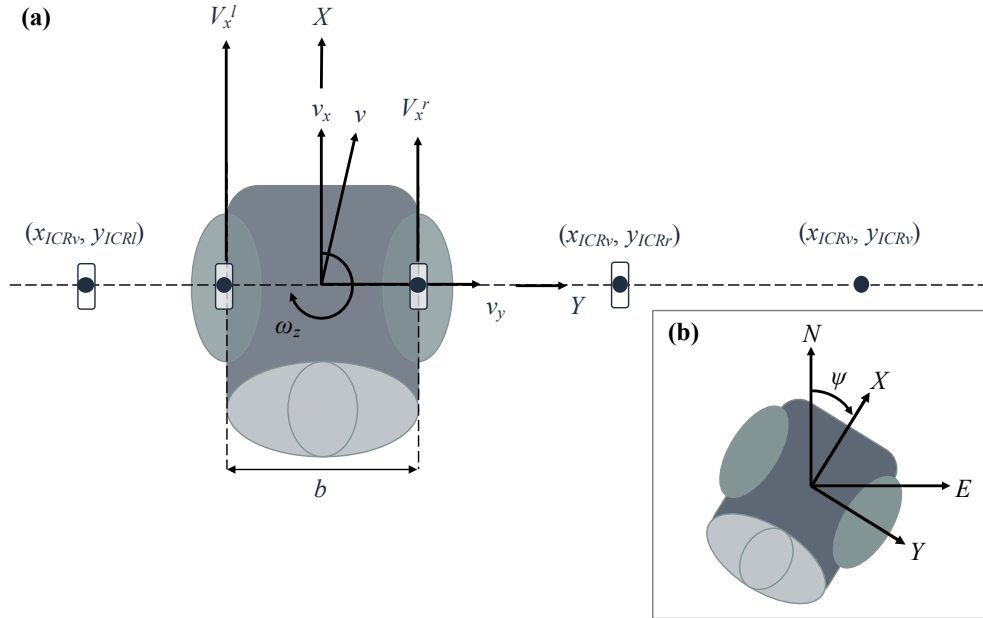


Figure 2: (a) ICR locations for the robotic wheelchair when undergoing slippage. (b) North-east-down coordinate frame with a positive clockwise heading angle.

where v_x and ω_z are the center of gravity longitudinal and angular velocities of the wheelchair, respectively. The lateral ICR locations between the right and left tires and the ground, y_{ICRl} and y_{ICRr} , respectively, are:

$$y_{ICRl} = -\frac{V_x^l - v_x}{\omega_z} \quad (2)$$

$$y_{ICRr} = -\frac{V_x^r - v_x}{\omega_z}, \quad (3)$$

where V_x^l and V_x^r are the velocities of the left and right tires relative to the body of the wheelchair, respectively. The longitudinal ICR location between the tires and the ground, x_{ICRv} , is given by:

$$x_{ICRv} = -\frac{v_y}{\omega_z}, \quad (4)$$

where v_y is the lateral velocity of the wheelchair. The longitudinal ICR locations between the left and right tires and the ground, x_{ICRl} and x_{ICRr} , can be computed similarly to Eqn. (2) and Eqn. (3), i.e.,

$$x_{ICRl} = \frac{V_y^l - v_y}{\omega_z} \quad (5)$$

$$x_{ICRr} = \frac{V_y^r - v_y}{\omega_z}. \quad (6)$$

However, since the wheelchair tires are nonholonomically constrained, the velocity in the Y direction is assumed to be zero, simplifying Eqn. (5) and Eqn. (6) to:

$$x_{ICRr} = x_{ICRl} = x_{ICRv} = -\frac{v_y}{\omega_z}. \quad (7)$$

Equations (2)-(4) can then be solved simultaneously for the wheelchair's longitudinal, lateral, and angular velocities, v_x , v_y , and ω_z , respectively, as a function of left and right wheel speeds, V^l and V^r .

$$v_x = \frac{V_x^r y_{ICRl} - V_x^l y_{ICRr}}{y_{ICRl} - y_{ICRr}} \quad (8)$$

$$v_y = \frac{(V_x^l - V_x^r)x_{ICRv}}{y_{ICRl} - y_{ICRr}} \quad (9)$$

$$\omega_z = -\frac{V_x^l - V_x^r}{y_{ICRl} - y_{ICRr}} \quad (10)$$

The EKF discussed in Section 3 is founded upon Eqns. (8)-(10) in order to predict the ICR locations.

3 EKF Estimation of ICR Locations

The EKF presented in this section has been derived in [22] to identify the ICR locations of tracked and wheeled skid-steer vehicles using inputs of track and wheel speeds as well as vehicle position and heading. For this work, the EKF algorithm incorporates input measurements of wheelchair position and orientation. A fixed north-east-down (NED) frame with a positive clockwise heading angle ψ is used, an illustration of the coordinate frame can be seen in Fig. 2 (b).

The wheelchair longitudinal and lateral velocities are presented in Eqns. (8)-(10). Using these velocities, the wheelchair velocities components in the north and east directions, \dot{N} and \dot{E} , respectively, can be defined as:

$$\dot{N} = v_x \cos(\psi) - v_y \sin(\psi) \quad (11)$$

$$\dot{E} = v_x \sin(\psi) + v_y \cos(\psi). \quad (12)$$

Augmenting Eqns. (10), (11), and (12) and assuming that the ICR locations remain constant results in the following continuous-time kinematic motion model:

$$\begin{bmatrix} \dot{N} \\ \dot{E} \\ \omega_z \\ \dot{y}_{ICRr} \\ \dot{y}_{ICRl} \\ \dot{x}_{ICRv} \end{bmatrix} = \begin{bmatrix} v_x \cos(\psi) - v_y \sin(\psi) + w_N \\ v_x \sin(\psi) + v_y \cos(\psi) + w_E \\ -\frac{V_x^l - V_x^r}{y_{ICRl} - y_{ICRr}} + w_\omega \\ w_r \\ w_l \\ w_x \end{bmatrix}. \quad (13)$$

Discretizing Eqn. (13) we obtain the discrete-time kinematic motion model:

$$\begin{bmatrix} N_k \\ E_k \\ \Psi_k \\ y_{ICRr_k} \\ y_{ICRl_k} \\ x_{ICRv_k} \end{bmatrix} = \begin{bmatrix} N_{k-1} + \Delta t V_{N_{k-1}} + \Delta t w_N \\ E_{k-1} + \Delta t V_{E_{k-1}} + \Delta t w_E \\ \Psi_{k-1} + \Delta t \omega_{\omega_{k-1}} + \Delta t w_{\omega} \\ y_{ICRr_{k-1}} + \Delta t w_r \\ y_{ICRl_{k-1}} + \Delta t w_l \\ x_{ICRv_{k-1}} + \Delta t w_x \end{bmatrix}, \quad (14)$$

where Δt is the time step and ω_E , ω_N , ω_ω , ω_r , ω_l , and ω_x are additive zero-mean Gaussian process noises. It has been previously shown that the ICR locations for vehicles traveling at low speeds on hard, flat terrain, which is the most common case for wheelchairs, remain within a small bounded region [22, 24]. Consequently, the ICR locations can be modeled as constants disturbed by random noise.

Once the discrete-time kinematic motion model has been defined, the EKF prediction step can be carried out using the standard EKF equations shown in (15) and (16):

$$\mathbf{x}_k^- = \mathbf{f}(\mathbf{x}_{k-1}^+, \mathbf{u}_{k-1}, 0) \quad (15)$$

$$\mathbf{P}_k^- = \mathbf{F}_{k-1} \mathbf{P}_{k-1}^+ \mathbf{F}_{k-1}^T + \mathbf{L}_{k-1} \mathbf{Q} \mathbf{L}_{k-1}^T, \quad (16)$$

where \mathbf{x}_k^- represents the propagated state at the current time step, \mathbf{x}_{k-1}^+ is the propagated and updated state from the previous time step, and \mathbf{u}_{k-1} is the input vector of wheelchair position, orientation, and individual wheel velocities. The third term in Eqn. (15) conveys the assumed zero process noise associated with the prediction step. The state covariance matrix, \mathbf{P} , is propagated using the Jacobian matrices \mathbf{F}_{k-1} and \mathbf{L}_{k-1} , as well as the process noise covariance of the motion model, \mathbf{Q} ,

$$\mathbf{F}_{k-1} = \frac{\partial \mathbf{f}_{k-1}}{\partial \mathbf{x}}|_{\mathbf{x}_{k-1}^+} \quad (17)$$

$$\mathbf{L}_{k-1} = \frac{\partial \mathbf{f}_{k-1}}{\partial \mathbf{w}}|_{\mathbf{x}_{k-1}^+} = \Delta t \mathbf{I}_{6 \times 6}. \quad (18)$$

The state measurement is updated via measurements of the wheelchair's position and orientation, N , E , and Ψ , respectively, the collection of which will be discussed in Section 5. These measurements are concatenated into the measurement vector \mathbf{y} .

$$\mathbf{y}_k = \begin{bmatrix} N_k \\ E_k \\ \Psi_k \end{bmatrix} \quad (19)$$

The direct measurements of the states yield the measurement equations in Eqn. (20):

$$\mathbf{h}_k = \begin{bmatrix} N + v_N \\ E + v_E \\ \Psi + v_\Psi \end{bmatrix}, \quad (20)$$

where v_N , v_E , and v_Ψ represent additive measurement noise.

Finally, with the Jacobians of the state model and prediction computed and the updates to the state estimate calculated, the correction step to the state estimate and covariance can be performed using the standard EKF equations, shown in 21, 22, and 23:

$$\mathbf{K}_k = \mathbf{P}_k^- \mathbf{H}_k^T (\mathbf{H}_k \mathbf{P}_k^- \mathbf{H}_k^T + \mathbf{M}_k \mathbf{R}_k \mathbf{M}_k^T)^{-1} \quad (21)$$

$$\mathbf{x}_k^+ = \mathbf{x}_k^- + \mathbf{K}_k [\mathbf{y}_k - h_k(\mathbf{x}_k^-, 0)] \quad (22)$$

$$\mathbf{P}_k^+ = (\mathbf{I}_{6 \times 6} - \mathbf{K}_k \mathbf{H}) \mathbf{P}_k^- . \quad (23)$$

Here \mathbf{H}_k and \mathbf{M}_k are Jacobian matrices for the measurement model and are given in Eqn. (24) and Eqn. (25), R is the measurement noise covariance of the measurement model, and y_k is the actual obtained measurements.

$$\mathbf{H}_k = \frac{\partial \mathbf{h}_k}{\partial \mathbf{x}}|_{\mathbf{x}_k^-} = \begin{bmatrix} 1 & 0 & 0 & 0 & 0 & 0 \\ 0 & 1 & 0 & 0 & 0 & 0 \\ 0 & 0 & 1 & 0 & 0 & 0 \end{bmatrix} \quad (24)$$

$$\mathbf{M}_k = \frac{\partial \mathbf{h}_k}{\partial \mathbf{v}}|_{\mathbf{x}_k^+} = \Delta t \mathbf{I}_{3 \times 3} \quad (25)$$

4 Simulation

To quantify how the ICR EKF algorithm performs under controlled conditions, the wheelchair's motion is implemented in simulation via the kinematic motion model presented in Eqn. (14). The ICRs were initialized at their true locations directly beneath the wheelchair's wheels, such that $y_{ICRr} = 0.245$ m, $y_{ICRI} = -0.245$ m, and $y_{ICRl} = 0.0$. The path of the simulated wheelchair, shown in Fig. 3 (a), incorporates straight-line motion and 90-degree turns in order to observe the ICR locations for both slip and non-slip conditions. The path is varied by adding zero-mean Gaussian noise to the left and right wheel velocity inputs, as well as by the measurement and process noise parameters. These additional noise parameters were obtained through experimental tuning. Supplementary bias was also added to the right or left wheel velocity inputs at various time periods to simulate tire slip. The simulation was initialized such that the locations at which the wheelchair experienced slip could be adjusted.

The results of the simulation are presented in Fig. 3. These results verify that the ICR locations do not vary significantly under simulated non-slip surfaces. However, the ICR locations do change significantly in simulated slip scenarios. This effect can be seen in Fig. 3 (c). In simulation, the maximum ICR errors are 0.30 m, 0.25 m, and 0.48 m for y_{ICRr} , y_{ICRI} , and x_{ICRv} , respectively. Via slip prediction, the EKF can more accurately predict the simulated wheelchair's position and orientation than two-wheeled robot kinematics alone (simulated odometry), as shown in Fig. 3 (a)-(b). A 1- σ RMS error of

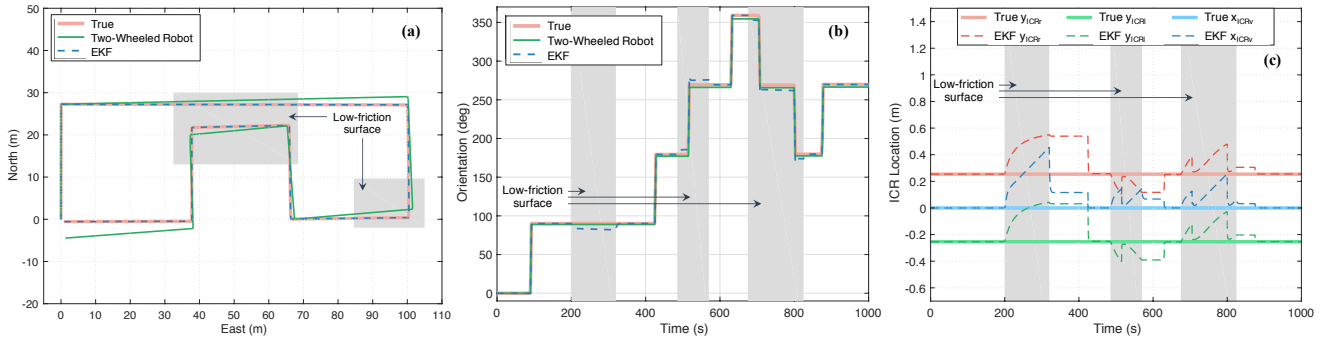


Figure 3: Results of simulation with low-friction surfaces shown in grey: (a) Comparison of the simulated wheelchair’s true position, two-wheeled robot model position, and the EKF estimated position; (b) Comparison of the simulated wheelchair’s true orientation, two-wheeled robot model orientation, and the EKF estimated orientation; (c) Comparison of the simulated wheelchair’s true ICR locations and the ICR EKF location estimates.

1.18E-06 degrees was observed between the simulated wheelchair’s true heading and the EKF’s predicted heading, while a 1- σ root-mean-squared (RMS) error of 11.03 degrees was observed between the simulated wheelchair’s true heading and the estimated heading of the two-wheeled robot. In addition, 1- σ RMS errors of only 1.25E-06 m in the North direction and 5.61E-07 m in the East direction were observed between the true wheelchair position and that of the EKF’s estimated position, depicted in Fig. 3 (a). However, when comparing the true position to the two-wheeled robot kinematics under high angular rate and slip conditions, a 1- σ RMS error of 7.14 m with a maximum error of 17.30 m in the North direction and a 1- σ RMS error of 2.42 m with a maximum error of 5.43 m in the East direction occurred.

It should be noted that the convergence time of the filter is highly dependent on the motion of the wheelchair. If the wheelchair is driven perfectly straight, the ICR estimates will not be updated. Rather, the ICR locations are learned while the angular rate is nonzero, which occurs when the wheelchair turns. The convergence time is also dependent upon the initialized ICR locations. For the remainder of this work, the convergence time is defined as the time it takes the ICR values to stay within five percent of their steady-state values. The ICR values are measured as a percentage of the total distance from the initial to the steady-state value. If the ICR values are initialized at their true locations, they will converge quickly, as in the case of the simulation, in which they converged almost immediately to their true values.

5 Experimental Implementation

A real-time implementation of the algorithm is useful to confirm the repeatability of the technique in the real-world, especially given that the assumptions made in the simulation or the convergence of the filter may not be entirely valid with real-world noise and disturbances. The algorithm was next implemented in real-time on a modified Jazzy Pride Select 6 wheelchair (Mobility Products Corp., USA), shown in Fig. 4, to demonstrate that the ICR EKF approach works in practice. An on-board computer serves as the principal interface between the joystick, sensors, motor controller, and Robot Operating System (ROS) used to control the wheelchair. An open-source, planar laser odometry package, RF2O, is utilized to obtain position and orientation measurements via a SICK LMS511 scanning laser rangefinder [28]. HB6M Hollow Bore Optical Encoders (US Digital, USA) are used to collect the wheelchair wheel velocities data, as well as wheel odometry.

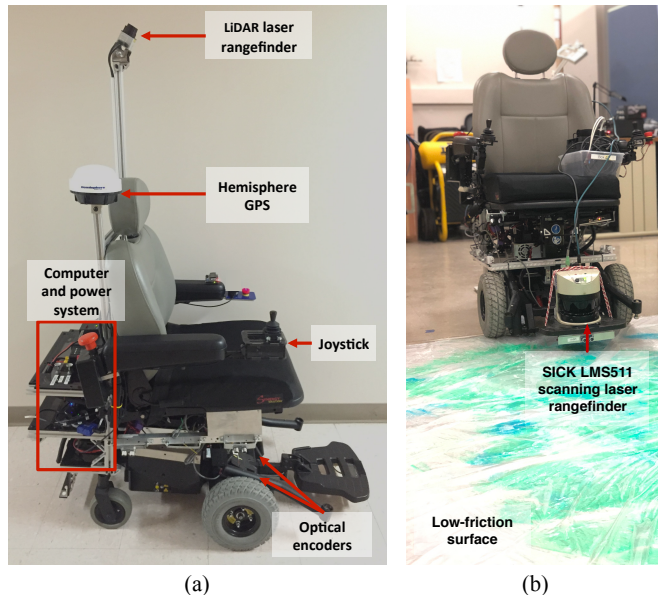


Figure 4: Robotic wheelchair used for experimentation: (a) Measurements of wheel velocities are obtained from the optical encoders; (b) Slip testing environment with measurements of wheelchair position and orientation obtained via laser odometry using a scanning laser rangefinder.

The odometry-based predictions provided by the encoders are then compared to the wheelchair position and orientation measurements of the ICR EKF algorithm. Additionally, the proposed ICR EKF approach is compared to a standard EKF using Eqns. 13 and 14 without the last three ICR rows in order further substantiate the contribution of the proposed algorithm.

Two experiments were performed to validate the ICR EKF algorithm, as well as to analyze the data in two separate ways. In Experiment 1, a slip-based data analysis was performed that highlights the ability of the algorithm to converge with incorrect initialization. In Experiment 2, a motion prediction analysis was performed that highlights the benefits of the ICR EKF strategy. In Experiment 1, the wheelchair was first driven on a surface where the tires would not slip to allow the ICR location estimates to converge to their true locations and then driven over a low-friction surface to induce slip on the tires. The wheelchair's path is shown in Fig. 5 (a). The non-slip surface consisted of common linoleum flooring. The low-friction surface was accomplished using large plastic sheeting coated with Dawn and Palmolive Ultra Strength dish soap. For Experiment 1, the ICR locations were initialized at 1.0 m, -1.0 m, and 0.2 m for y_{ICRr} , y_{ICRI} , and x_{ICRv} , respectively. The ICR locations were initialized at these values to observe the response of the algorithm when the true ICR locations are not known.

In Experiment 2, the wheelchair was driven in paths similar to that of Experiment 1 and the correct ICR locations were used for initialization, but demonstrates the ICR EKF's ability to predict the motion of the wheelchair during slip, as shown in Fig. 7: (a) the wheelchair undergoing slip to the right, (b) the wheelchair undergoing slip to the left, and (c) the body of the wheelchair slipping forward. The ICR locations were initialized to lie directly beneath the wheelchair's drive wheels, the true locations for a two-wheeled robot. The initial ICR locations for the wheelchair are 0.254 m, -0.254 m, and 0.0 m for y_{ICRr} , y_{ICRI} , and x_{ICRv} , respectively. The experimental results are presented in the following sections.

6 Results

This section presents the results of Experiment 1 and Experiment 2. The results of Experiment 1 are presented and discussed in Section 6.1. The results of Experiment 2 are presented and discussed in Section 6.2.

6.1 Experiment 1: ICR EKF Performance

Experiment 1 was conducted to observe the performance of the ICR EKF algorithm even in situations where the algorithm is initialized with values other than the true ICR locations. Over twenty trials were collected with similar results. For simplicity, only one trial’s full ICR estimate results will be presented in this paper. The results of Experiment 1 can be seen in Fig. 5.

The results shown in Fig. 5 are as follows: Fig. 5 (a) illustrates the path driven by the wheelchair as measured by laser odometry, wheel odometry, estimated by a standard EKF with no ICR estimates (i.e. using Eqns. 13 and 14 without the last three ICR rows), and estimated by the ICR EKF, which the low-friction surface shown in grey. Each turn is represented by an encircled number and the two laps are labeled. In Fig. 5 (b), the orientation of the wheelchair (top), as measured by laser odometry, wheel odometry, estimated by a standard EKF with no ICR estimates, and estimated by the ICR EKF, as well as the velocity of the wheelchair (bottom), as measured by laser odometry and wheel odometry, are shown. The yawrate comparison for laser odometry, wheel odometry, the standard EKF, and the ICR EKF is presented in Fig. 5 (c). The moments in which the wheelchair turned are again represented by encircled numbers, which repeat for the second lap (labeled within the figure).

A comparison of the experienced magnitude of slip for the right wheel, left wheel, and wheelchair body is presented in Fig. 5 (d) and (e). A significant increase in slipping ratio was observed as the wheelchair traveled over the low-friction surface, shown in grey, for both laps. The changes in slipping ratio per tire and for the wheelchair chassis are also apparent in the two figures.

Finally, the estimated wheelchair left, right, and longitudinal ICR locations during the experiment are depicted in Fig. 5 (f). Once the algorithm converged, and when the wheelchair was not being driven on the low-friction surface, it was observed that the ICR locations vary within 2σ standard deviations of 0.057 m, 0.076 m, 0.043 m, with maximum deviations of 0.090 m, 0.085 m, and 0.078 m for y_{ICRr} , y_{ICRI} , and x_{ICRv} , respectively, from the true ICR locations. During slip, the maximum ICR deviations are 0.79 m, 0.84 m, and 0.26 m for y_{ICRr} , y_{ICRI} , and x_{ICRv} , respectively, from the true ICR locations. These results are 8.83, 9.88, and 3.30 times larger than the maximum deviation seen when the wheelchair is not experiencing slip. These results can then be compared to the slipping ratio for the right wheel, left wheel, and wheelchair chassis presented in Fig. 5 (e). Comparing Fig. 5 (e) and (f), it is observed that the slipping ratios are indeed increasing as the wheelchair undergoes slippage, validating the deviations of the ICR locations observed at the same locations. Moreover, the magnitude of slip in Fig. 5 (e) is comparable to the ICR deviations between the right wheel and y_{ICRr} , the left wheel and y_{ICRI} , as well as the wheelchair body and x_{ICRv} , respectively.

The algorithm’s convergence period and the resulting convergence times are also seen in Fig. 5 (f). Initializing the algorithm with arbitrary ICR locations results in convergence times of 14.10, 14.10, and 14.35 seconds for y_{ICRr} , y_{ICRI} , and

x_{ICRv} , respectively. These convergence times average approximately 2.70 times, or 41%, longer than when the algorithm is initialized with the true ICR locations, as will be discussed later in this section. Consequently, if the algorithm is incorrectly initialized, useful predictions of wheel slip may not be accurately provided until the ICR locations have converged. Typically, one would expect that the initialization of ICR positions from incorrect values would only occur during the first operation of the wheelchair, or rarely occur because initial estimates could be forced to be underneath the wheels – as is typical in normal no-slip operation.

Additionally, it was found that convergence times are strongly dependent on the motion of the wheelchair. If the wheelchair is driven perfectly straight, the ICR estimates cannot be updated. The ICR locations will only converge quickly from incorrect initial values if the wheelchair is driven with a nonzero angular rate.

The results shown in Fig. 5 (a), (b), and (c) present the improvement of the algorithm’s estimate and prediction of position, orientation, and yawrate in comparison to odometry alone, as well as in comparison the standard EKF. The ICR EKF algorithm estimates the position of the wheelchair within an error of 0.118 m in terms of Euclidean distance. Conversely, the maximum odometry Euclidean distance error is 1.217 m, and the maximum standard EKF Euclidean distance error is 0.160 m. When comparing the orientation errors for the ICR EKF, odometry, and the standard EKF, maximum errors of 7.7 degrees, 102.5 degrees, and 11.3 degrees, were found, respectively. Similarly, the ICR EKF algorithm estimates the yawrate of the wheelchair within an error of 0.380 rad/s, while the maximum odometry measurement error is over twice that at 0.934 rad/s, and the maximum standard EKF measurement error is 1.255 rad/s. The ICR convergence period can be seen as an increasing error in the EKF’s predicted wheelchair yawrate from the laser odometry-based ground truth’s more accurate estimate of the wheelchair’s yawrate.

Moreover, to justify the assumption that the ICRs are affected by zero-mean Gaussian noise, a histogram of the ICR locations for multiple trials is presented in Fig. 6. The top subplot shows the ICR locations for no-slip conditions, while the bottom subplot shows the ICR locations while the wheelchair is experiencing slip. From Fig. 6, the hypothesis that each of the ICR locations remain within a small bounded region is validated, especially during no-slip conditions. The distributions are also seen to be Gaussian. Finally, an interesting aspect to note in this figure is the bias of the ICR locations to the right. This bias may in part be due to un-modeled dynamics, such as friction. However, the more likely cause of the bias is that the wheelchair only made left turns during the trials used to create the histograms. Consequently, an unforeseen result of the proposed algorithm may be the predicted direction of turn by the wheelchair from the ICR location estimates.

6.2 Experiment 2: ICR EKF Motion Prediction

Experiment 2 was conducted to observe the ICR EKF algorithm’s prediction of wheelchair motion during slip. In addition, Experiment 2 demonstrates the repeatable performance of the ICR EKF algorithm for different slip cases: the wheelchair slipping to the right, the wheelchair slipping to the left, and the body of the wheelchair slipping forward. The results of Experiment 2 are presented in Fig. 7.

For this work, the magnitude of slip is defined as:

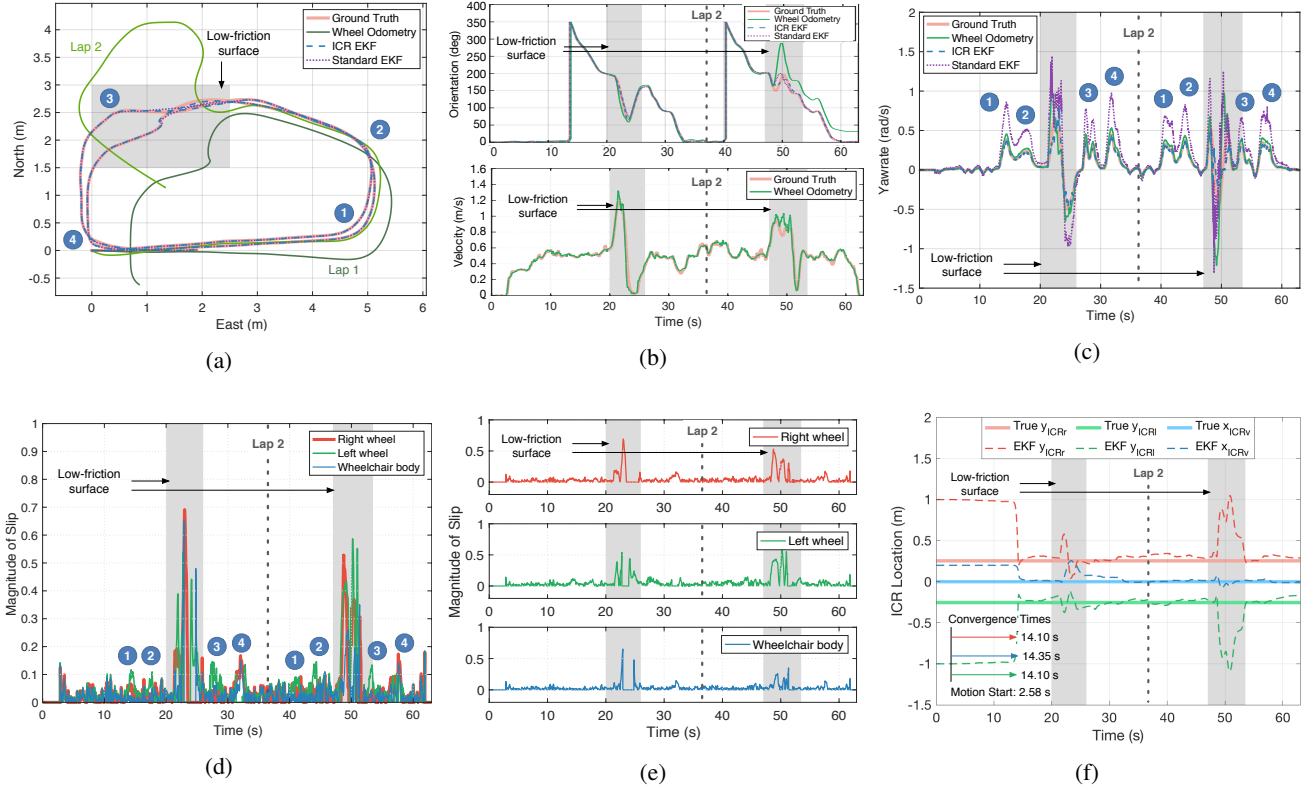


Figure 5: Results of Experiment 1 with low-friction surfaces shown in grey: (a) Comparison of the wheelchair's position from laser odometry-based ground truth, wheel odometry, a standard EKF, and the ICR EKF, respectively; (b) Comparison of the wheelchair's orientation from laser odometry, wheel odometry, a standard EKF, and the ICR EKF, respectively (top), and a comparison of the wheelchair's velocity from laser odometry and wheel odometry, respectively (bottom); (c) Comparison of the wheelchair's yawrate from laser odometry, wheel odometry, a standard EKF, and the ICR EKF, respectively; (d) Comparison of magnitude of slip for the wheelchair's right wheel, left wheel, and body, respectively; (e) Magnitude of slip for the wheelchair's right wheel (top), left wheel (middle), and body (bottom); (f) Comparison of the wheelchair's true ICR locations and the ICR EKF location estimates.

$$||\lambda_{r,l}|| = \frac{V_x^{r,l} - v_x}{v_x}, \quad (26)$$

where $V_x^{r,l}$ represents the wheelchair's right or left wheel velocity and v_x is the longitudinal velocity of the wheelchair. It should be noted that equation (26) fails under two conditions: 1) the wheelchair is stationary with no forward longitudinal velocity ($V_x^{r,l} = v_x = 0$) and thus Eqn. (26) approaches infinity; and 2) the wheelchair is turning in place with no forward longitudinal velocity ($v_x = 0$) and again Eqn. (26) approaches infinity.

The slip equation can then be rearranged and solved in terms of wheel velocity:

$$V_x^{r,l} = v_x(1 + \lambda_{r,l}). \quad (27)$$

Next, Eqn. (27) can be substituted into the ICR kinematic equations, such that Eqn. (2) and Eqn. (3), respectively, become

$$y_{ICRl} = -\frac{v_x \lambda_l}{\omega_z} \quad (28)$$

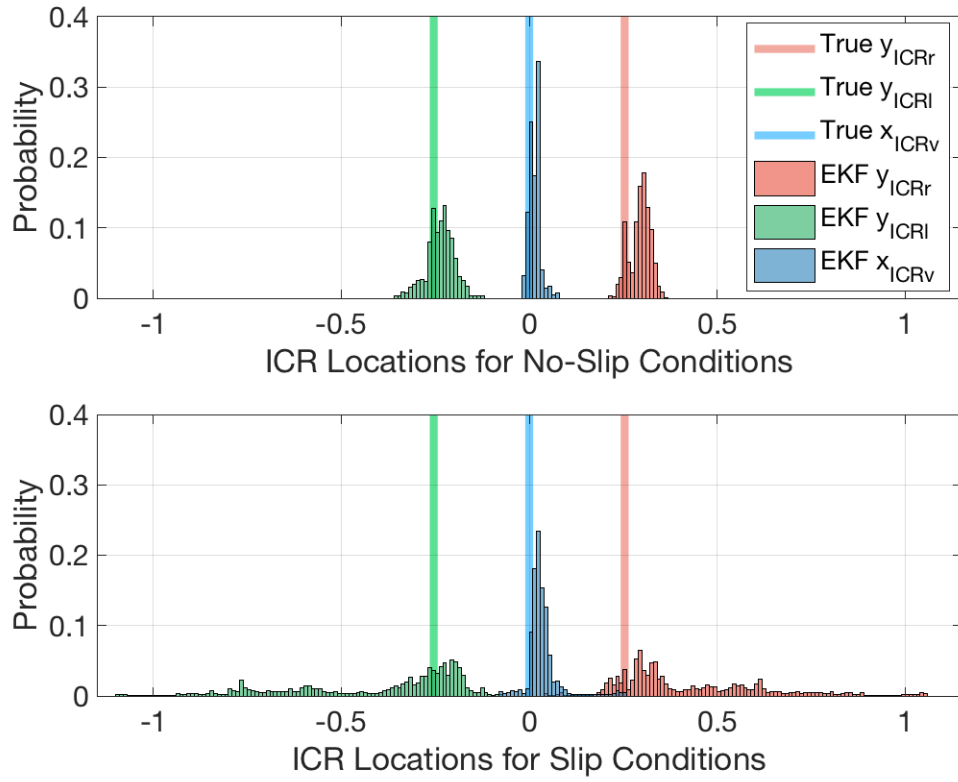


Figure 6: Histogram of ICR locations for no-slip conditions (top) and slip conditions (bottom).

$$y_{ICRr} = -\frac{v_x \lambda_r}{\omega_z}, \quad (29)$$

and x_{ICRv} remains the same. Substituting Eqns. (27)-(29) into the kinematic motion model, we ultimately find that each state equation remains the same as the original kinematic model presented in Eqn. (13), except for that of angular rate, ω_z . When replacing the right and left wheel velocities with wheel slip (Eqn. (26)), the equation for angular rate becomes a degenerate case in which

$$\omega_z = w_z. \quad (30)$$

Therefore, utilizing wheel slip as the inputs to the ICR kinematic equations will yield the same result as inputs of wheel velocities, apart from Eqn. (30). However, the secondary contribution of this paper is that the ICR EKF provides a model-based framework to predict motion as the wheelchair experiences slip, which cannot be achieved through slip-based measurement alone.

To demonstrate the model-based predictions during slip, the three motion cases are presented in Fig. 7: (a) the wheelchair slipping to the right, (b) the wheelchair slipping to the left, and (c) the body of the wheelchair slipping forward. An enhanced view of each of these cases is presented in Fig. 7 (d)–(f), respectively. The instantaneous slip vectors represent the predicted differences in the actual versus intended motion of the wheelchair. In particular, it was observed that wheel slip may not always occur on a low-friction surface. Indeed, with typical wheelchair applications, the user would most likely prefer that

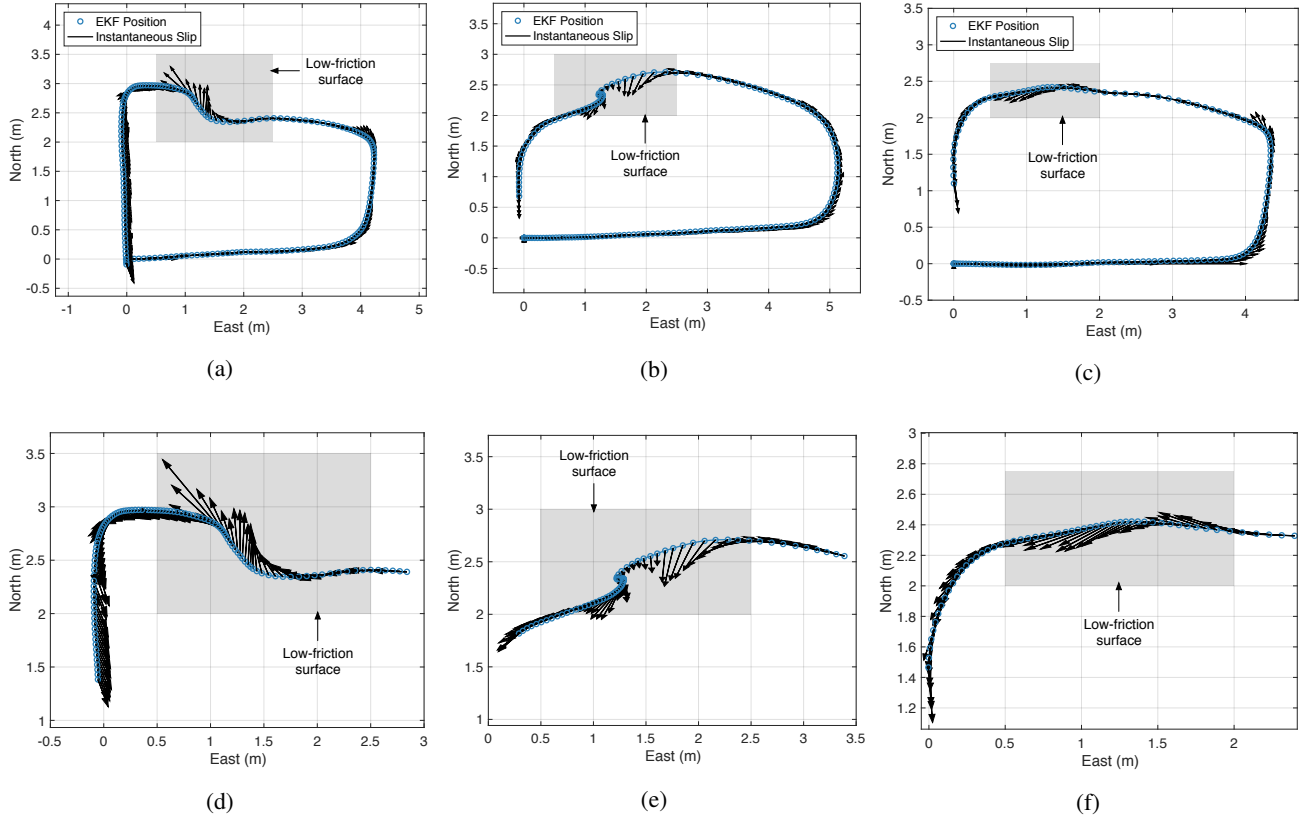


Figure 7: Results of Experiment 2 with low-friction surfaces shown in grey. Prediction of wheelchair motion during slip for three cases: (a) Wheelchair undergoing slip to the right; (b) Wheelchair undergoing slip to the left; (c) Body of the wheelchair slipping forward; (d) Enhanced view of wheelchair undergoing slip to the right; (e) Enhanced view of wheelchair undergoing slip to the left; (f) Enhanced view of wheelchair body slipping forward.

the wheelchair does not frequently experience slip, even on low-friction surfaces. For example, Fig. 7 (a) and (d) demonstrate a scenario in which the wheelchair does not purely experience slip on the low-friction surface. However, the algorithm can still accurately differentiate between situations when the wheelchair is and is not experiencing slip.

7 Discussion

The experimental results further validate what is observed in simulation in that the ICR locations are not found to experience significant deviation from their steady-state values when the wheelchair is operated under low-slip surface conditions. The results in Fig. 5 (f) demonstrate how the ICR locations do not deviate significantly under normal operating conditions, but change dramatically during slippage. These ICR locations can be learned during normal operating behavior of the wheelchair because this is assumed to be the typical function. Thereafter, if significant changes are seen in the ICR locations, this implies the presence of potentially dangerous slip, as seen in Fig. 7, which can be used to develop responses to enhance wheelchair safety. For example, when error is present between the true and estimated ICR values, the wheelchair system can enter a slip-safe operational mode, ranging from simply limiting the top speed to implementing an anti-skid system onboard the wheelchair, analogous to anti-lock brakes on passenger vehicles.

Of particular importance is the dependence of the ICR convergence time on both EKF initialization and wheelchair

motion. As mentioned in Section 4 and in the discussion of Experiment 1 in this section, the convergence time of the algorithm is also highly dependent upon the motion of the wheelchair; a nonzero angular rate is necessary for the algorithm to learn the ICR locations. In Experiment 1, the ICR estimates undergo a brief increase in error prior to converging. Due to incorrect initial ICR estimates, a larger increase in error is observed prior to ICR convergence in Experiment 1.

The results of Experiment 2 demonstrate that the algorithm predicts the motion of the wheelchair even during slippage, shown in Fig. 7. In both experiments, the ICR locations return very quickly to their true locations after the wheelchair is driven off the low-friction surface and back onto the high-friction surface. The ICR locations will then only change significantly when the wheelchair tires are undergoing slip.

From the results of the two experiments, it was also observed that the prediction of the wheelchair’s position and slip is improved with the implementation of the ICR EKF algorithm in contrast to odometry alone. This result is clearly seen in comparisons of the wheelchair’s true position (as provided by laser odometry-based localization), wheel odometry-based position measurements, and the EKF estimated position for each experiment. The position comparisons are depicted for Experiment 1 and Experiment 2 in Fig. 5 (a) and Fig. 7, respectively. While the wheelchair is driven on a non-slip surface, the EKF algorithm prediction and odometry measurements closely track the map-based localization estimates. However, as the wheelchair traverses the low-friction surface and the ICR locations have converged to approximately their true locations, the EKF algorithm demonstrates significant improvement in estimating the position of the wheelchair when compared to the use of odometry alone.

8 Conclusions

This paper is concerned with improving the safety of wheelchair operation by the estimation of wheelchair motion in the presence of significant slip. The results of this research demonstrate the application of ICR estimation for a wheelchair under situations where ICR locations should not typically change in order to estimate wheelchair tire slip in real-time, as well as a model-based framework to predict motion during that slip. For the two experiments presented within this paper, while the wheelchair is driven on the non-slip surface, it was shown that the ICR locations do not vary significantly under the slip-free conditions of normal operation and were tracked with 2σ standard deviations of 0.057 m, 0.076 m, and 0.043 m for y_{ICR_r} , y_{ICR_l} , and x_{ICR_v} , respectively. However, as the wheelchair tires experienced slip the maximum ICR discrepancies grew to as much as 0.79 m, 0.84 m, and 0.26 m for y_{ICR_r} , y_{ICR_l} , and x_{ICR_v} , respectively. This result is 8.83, 9.88, and 3.30 times larger than the maximum error seen when the wheelchair is not experiencing slip. This result is significant because the changing ICR values indicative of slip can be utilized to enable warning systems and slip-safe operational modes.

It is shown that the algorithm most quickly converges when the EKF is initialized with the true ICR estimates, resulting in minimal deviations in the ICR locations. However, the estimates converged regardless of the initial estimate.

In addition, odometry errors are particularly susceptible to low-friction surfaces, often representative of dangerous operational conditions. The implementation of the ICR EKF for a distance of approximately 6 m over slip surfaces resulted in maximum position errors of 0.11 m for the EKF algorithm, compared to 1.22 m for odometry. The ICR EKF algorithm estimated the wheelchair’s yawrate within a maximum error of 0.38 rad/s, while the maximum odometry measurement error was 0.93 rad/s. Consequently, the predicted position and yawrate of the wheelchair is improved when utilizing the ICR EKF

estimates in contrast to pure odometry. Moreover, the implementation of this method with electric powered wheelchairs can enhance the prediction of wheelchair motion when undergoing slip, thus enabling warning systems and safe operational modes that can enhance the safety of wheelchair users.

Acknowledgements

This material is based upon work supported by the National Science Foundation under Grant No. DGE1255832. Any opinions, findings, and conclusions or recommendations expressed in this material are those of the authors and do not necessarily reflect the views of the National Science Foundation.

References

- [1] Wang, H., Salatin, B., Grindle, G. G., Ding, D., and Cooper, R. A., 2009. “Real-time model based electrical powered wheelchair control”. *Medical engineering & physics*, **31**(10), pp. 1244–1254.
- [2] Ummat, S., and Kirby, R. L., 1994. “Nonfatal wheelchair-related accidents reported to the national electronic injury surveillance system.”. *American journal of physical medicine & rehabilitation*, **73**(3), pp. 163–167.
- [3] Ding, D., and Cooper, R. A., 2005. “Electric powered wheelchairs”. *Control Systems, IEEE*, **25**(2), pp. 22–34.
- [4] Brault, M. W., of the Census, U. S. B., et al., 2012. *Americans with disabilities: 2010*. US Department of Commerce, Economics and Statistics Administration, US Census Bureau.
- [5] Bentley, T. A., 1998. “Slip, trip and fall accidents occurring during the delivery of mail”. *Ergonomics*, **41**(12), pp. 1859–1872.
- [6] Gao, C., and Abeysekera, J., 2004. “Slips and falls on ice and snow in relation to experience in winter climate and winter sport”. *Safety science*, **42**(6), pp. 537–545.
- [7] Lemaire, E. D., O’Neill, P. A., Desrosiers, M. M., and Robertson, D. G., 2010. “Wheelchair ramp navigation in snow and ice-grit conditions”. *Archives of physical medicine and rehabilitation*, **91**(10), pp. 1516–1523.
- [8] Xiang, H., Chany, A., and Smith, G. A., 2006. “Wheelchair related injuries treated in us emergency departments”. *Injury prevention*, **12**(1), pp. 8–11.
- [9] Rousseau, J., Aissaoui, R., and Bourbonnais, D., 2005. “Measuring the effort needed to climb access ramps in a manual wheelchair”. *CMHC-SCHL Research Highlight*, pp. 1–4.
- [10] Gustafsson, F., 1997. “Slip-based tire-road friction estimation”. *Automatica*, **33**(6), pp. 1087–1099.
- [11] Helmick, D. M., Cheng, Y., Clouse, D. S., Matthies, L. H., and Roumeliotis, S. I., 2004. “Path following using visual odometry for a mars rover in high-slip environments”. In Aerospace Conference, 2004. Proceedings. 2004 IEEE, Vol. 2, IEEE, pp. 772–789.
- [12] Olson, C. F., Matthies, L. H., Schoppers, M., and Maimone, M. W., 2000. “Robust stereo ego-motion for long distance navigation”. In Computer Vision and Pattern Recognition, 2000. Proceedings. IEEE Conference on, Vol. 2, IEEE, pp. 453–458.

- [13] Reina, G., Ojeda, L., Milella, A., and Borenstein, J., 2006. “Wheel slippage and sinkage detection for planetary rovers”. *Mechatronics, IEEE/ASME Transactions on*, **11**(2), pp. 185–195.
- [14] Ward, C. C., and Iagnemma, K., 2007. “Model-based wheel slip detection for outdoor mobile robots”. In *Robotics and Automation, 2007 IEEE International Conference on*, IEEE, pp. 2724–2729.
- [15] Ward, C., and Iagnemma, K., 2008. “A dynamic-model-based wheel slip detector for mobile robots on outdoor terrain”. *Robotics, IEEE Transactions on*, **24**(4), pp. 821–831.
- [16] Milella, A., Reina, G., and Siegwart, R., 2006. “Computer vision methods for improved mobile robot state estimation in challenging terrains”. *Journal of multimedia*, **1**(7), pp. 49–61.
- [17] Nistér, D., Naroditsky, O., and Bergen, J., 2006. “Visual odometry for ground vehicle applications”. *Journal of Field Robotics*, **23**(1), pp. 3–20.
- [18] Song, X., Seneviratne, L. D., and Althoefer, K., 2011. “A kalman filter-integrated optical flow method for velocity sensing of mobile robots”. *Mechatronics, IEEE/ASME Transactions on*, **16**(3), pp. 551–563.
- [19] Song, X., Seneviratne, L., and Althoefer, K., 2011. “Slip parameter estimation for tele-operated ground vehicles in slippery terrain”. *Proceedings of the Institution of Mechanical Engineers, Part I: Journal of Systems and Control Engineering*, p. 0959651811401955.
- [20] Rogers-Marcovitz, F., George, M., Seegmiller, N., and Kelly, A., 2012. “Aiding off-road inertial navigation with high performance models of wheel slip”. In *Intelligent Robots and Systems (IROS), 2012 IEEE/RSJ International Conference on*, IEEE, pp. 215–222.
- [21] Pentzer, J., Brennan, S., and Reichard, K., 2014. “The use of unicycle robot control strategies for skid-steer robots through the icr kinematic mapping”. In *Intelligent Robots and Systems (IROS 2014), 2014 IEEE/RSJ International Conference on*, IEEE, pp. 3201–3206.
- [22] Pentzer, J., Brennan, S., and Reichard, K., 2014. “Model-based prediction of skid-steer robot kinematics using online estimation of track instantaneous centers of rotation”. *Journal of Field Robotics*, **31**(3), pp. 455–476.
- [23] Peacock, T., and Hadjiconstantinou, 2007. *Kinematics of Rigid Bodies: Instant Centers or Instantaneous Centers*, Vol. 2.003J/1.053J of *Lecture Notes in Dynamics and Control I*. MIT OpenCourseWare, Massachusetts Institute of Technology.
- [24] Martínez, J. L., Mandow, A., Morales, J., Pedraza, S., and García-Cerezo, A., 2005. “Approximating kinematics for tracked mobile robots”. *The International Journal of Robotics Research*, **24**(10), pp. 867–878.
- [25] Wolkowicz, K., Pentzer, J., Miller, C., Moore, J. Z., and Brennan, S. N., 2016. “On-line estimation of wheelchair tire slip utilizing an instantaneous center of rotation extended kalman filter”. In *ASME 2016 Dynamic Systems and Control Conference*, American Society of Mechanical Engineers, pp. V001T06A002–V001T06A002.
- [26] Kelly, A., and Seegmiller, N., 2014. “A vector algebra formulation of mobile robot velocity kinematics”. In *Field and Service Robotics*, Springer, pp. 613–627.
- [27] Mandow, A., Martinez, J. L., Morales, J., Blanco, J. L., Garcia-Cerezo, A., and Gonzalez, J., 2007. “Experimental kinematics for wheeled skid-steer mobile robots”. In *Intelligent Robots and Systems, 2007. IROS 2007. IEEE/RSJ*

- International Conference on, IEEE, pp. 1222–1227.
- [28] Jaimez, M., G. Monroy, J., and González-Jiménez, J., 2016. “Planar odometry from a radial laser scanner. a range flow-based approach”. In IEEE International Conference on Robotics and Automation (ICRA), pp. 4479–4485.

List of Figure Numbers and Respective Captions

Figure 1. Block diagram representing the signal flow of the system architecture.

Figure 2. (a) ICR locations for the robotic wheelchair when undergoing slippage. (b) North-east-down coordinate frame with a positive clockwise heading angle.

Figure 3. Results of simulation with low-friction surfaces shown in grey: (a) Comparison of the simulated wheelchair’s true position, two-wheeled robot model position, and the EKF estimated position; (b) Comparison of the simulated wheelchair’s true orientation, two-wheeled robot model orientation, and the EKF estimated orientation; (c) Comparison of the simulated wheelchair’s true ICR locations and the ICR EKF location estimates.

Figure 4. Robotic wheelchair used for experimentation: (a) Measurements of wheel velocities are obtained from the optical encoders; (b) Slip testing environment with measurements of wheelchair position and orientation obtained via laser odometry using a scanning laser rangefinder.

Figure 5. Results of Experiment 1 with low-friction surfaces shown in grey: (a) Comparison of the wheelchair’s position from laser odometry-based ground truth, wheel odometry, a standard EKF, and the ICR EKF, respectively; (b) Comparison of the wheelchair’s orientation from laser odometry, wheel odometry, a standard EKF, and the ICR EKF, respectively (top), and a comparison of the wheelchair’s velocity from laser odometry and wheel odometry, respectively (bottom); (c) Comparison of the wheelchair’s yawrate from laser odometry, wheel odometry, a standard EKF, and the ICR EKF, respectively; (d) Comparison of magnitude of slip for the wheelchair’s right wheel, left wheel, and body, respectively; (e) Magnitude of slip for the wheelchair’s right wheel (top), left wheel (middle), and body (bottom); (f) Comparison of the wheelchair’s true ICR locations and the ICR EKF location estimates.

Figure 6. Histogram of ICR locations for no-slip conditions (top) and slip conditions (bottom).

Figure 7. Results of Experiment 2 with low-friction surfaces shown in grey. Prediction of wheelchair motion during slip for three cases: (a) Wheelchair undergoing slip to the right; (b) Wheelchair undergoing slip to the left; (c) Body of the wheelchair slipping forward; (d) Enhanced view of wheelchair undergoing slip to the right; (e) Enhanced view of wheelchair undergoing slip to the left; (f) Enhanced view of wheelchair body slipping forward.